

# Silicon photonic microresonator-based high-resolution line-by-line pulse shaping

Received: 4 March 2024

Accepted: 24 August 2024

Published online: 09 September 2024

 Check for updatesLucas M. Cohen <sup>1</sup>✉, Kaiyi Wu <sup>1</sup>✉, Karthik V. Myilswamy <sup>1</sup>, Saleha Fatema <sup>1</sup>, Navin B. Lingaraju <sup>2</sup> & Andrew M. Weiner <sup>1</sup>

Optical pulse shaping stands as a formidable technique in ultrafast optics, radio-frequency photonics, and quantum communications. While existing systems rely on bulk optics or integrated platforms with planar waveguide sections for spatial dispersion, they face limitations in achieving finer (few- or sub-GHz) spectrum control. These methods either demand considerable space or suffer from pronounced phase errors and optical losses when assembled to achieve fine resolution. Addressing these challenges, we present a foundry-fabricated six-channel silicon photonic shaper using microresonator filter banks with inline phase control and high spectral resolution. Leveraging existing comb-based spectroscopic techniques, we devise a system to mitigate thermal crosstalk and enable the versatile use of our on-chip shaper. Our results demonstrate the shaper's ability to phase-compensate six comb lines at tunable channel spacings of 3, 4, and 5 GHz. Specifically, at a 3 GHz channel spacing, we showcase the generation of arbitrary waveforms in the time domain. This scalable design and control scheme holds promise in meeting future demands for high-precision spectral shaping capabilities.

By controlling the amplitude and phase of spectral lines over a coherent, broadband optical spectrum, optical pulse shaping has been widely used in applications for ultrafast optical arbitrary waveform generation<sup>1–6</sup>, wideband radio frequency (RF) photonics<sup>7–15</sup>, and manipulation of frequency-encoded photonic quantum information<sup>16–18</sup>. Fourier transform pulse shapers based on bulk optics comprise a pair of spectral dispersers with spatial light modulators between them. The first spectral disperser scatters, or demultiplexes, a broadband field such that individual spectral components are routed to unique light-modulating elements. Following modification of the amplitude and phase by the spatial light modulator, the spectral components are recombined, or multiplexed, at the second spectral disperser<sup>2</sup>. Commercially available pulse shapers rely on bulk spectral dispersers and liquid-crystal-on-silicon (LCoS) spatial light modulators to control the amplitude and phase of the input signal<sup>19,20</sup>. In laboratory settings, it is common to replace or pair diffraction gratings with virtually imaged phase arrays to enhance the spectral resolution<sup>21–23</sup>.

While off-the-shelf equipment is well-suited for femtosecond, high-repetition-rate optical waveform manipulation<sup>3</sup>, the technology has severe limitations when one requires finer control over the optical spectrum as is the case with low-repetition rate optical pulse shaping or high resolution spectrometry<sup>4</sup>. In particular, few- or sub-GHz addressability is invariably associated with a significant loss penalty and also requires an increase in the system size, which is prohibitive outside of the laboratory environment.

High resolution optical pulse shaping has proven invaluable across diverse quantum applications. The technology would enable straightforward manipulation and characterization of frequency-encoded photonic quantum information by reducing the separation between addressable modes in the computational space<sup>18,24</sup>. In addition, it facilitates fast waveform modulation to generate voltage standards traceable to fundamental quantum limits<sup>25</sup>, as well as precise control of optical transitions in ions or atoms<sup>25,26</sup>. Furthermore, high spectral resolution is vital in microwave photonics for generating and manipulating longer waveforms<sup>13,15</sup>. Fine-grained control over the

<sup>1</sup>School of Electrical and Computer Engineering, Purdue University, West Lafayette, IN 47907, USA. <sup>2</sup>The Johns Hopkins University Applied Physics Laboratory, Laurel, MD 20723, USA. ✉e-mail: [cohen26@purdue.edu](mailto:cohen26@purdue.edu); [wu1871@purdue.edu](mailto:wu1871@purdue.edu)

spectral amplitude also has tremendous value in applications where control over the spectral phase is not required. This is particularly true in spectroscopy, where high resolution spectral filtering has been used with Brillouin light-scattering techniques for non-invasive biological imaging<sup>27,28</sup> and to characterize stellar illumination in astrophotonics applications<sup>29,30</sup>.

As an enabling technology, photonic integrated circuits (PICs) offer a low size, weight, and power chip-scale platform for pulse shaping. The silicon-on-insulator (SOI) platform especially benefits from mature complementary metal-oxide-semiconductor (CMOS) process compatibility to enable a rich component ecosystem with the capability for volume production of complex PICs. Numerous on-chip shapers have been shown employing arrayed waveguide gratings (AWGs) as spectral dispersers<sup>31–35</sup>. However, to achieve a sub-GHz spectral resolution, AWG-based spectral dispersers require an excessively large ( $\sim\text{cm}^2$ ) device footprint which leads to increasing phase errors on platforms like SOI<sup>36</sup>. Also, AWGs do not offer tunability, which results in channel bandwidths and spacings that are fixed. To address these issues, shapers with a microresonator-based spectral disperser, whose channel bandwidth and minimum spacing depend on the quality (Q) factor of the microresonators, have been explored<sup>9,37,38</sup>. Although previous demonstrations have used microresonators with a low Q factor (linewidth  $\sim 8$  GHz or greater), microresonators on SOI can be designed to be extremely wavelength selective with a high Q factor of  $>10^6$ <sup>39,40</sup> and can be realized with a small device footprint of  $\sim 10^{-2}$  mm<sup>2</sup>. Their center frequency can be tuned via the thermo-optic (TO), free-carrier dispersion, or other dispersive effects. TO tuning is common because it offers simple design and fabrication, a wide tuning range, and does not fundamentally induce optical loss. However, thermal crosstalk introduces challenges in the large-scale control of such shapers.

In this paper, we design, fabricate, and optimize high-resolution ( $\sim 900$  MHz linewidth) microresonator filter banks with inline phase control for narrowband pulse shaping. We demonstrate a method of accurately aligning such shapers onto arbitrary frequency grids with any prescribed phase. In particular, we combine multi-heterodyne spectroscopy (MHS)<sup>41</sup> and dual-comb spectroscopy (DCS)<sup>42</sup> to sample channel frequencies and phases over short acquisition times and with high spectral resolution. This allows real-time monitoring of the

system response and accurate tuning of the shaper elements in the presence of thermal crosstalk or environmental disturbances. We employ our method with a six-channel silicon photonic (SiP) device with sub-GHz channel linewidths programmed to operate on a 3 GHz grid to synthesize arbitrary user-defined optical waveforms in the time domain. We emphasize the tunability of our shaper by extending the waveform demonstrations to 4 and 5 GHz frequency grids to phase-compensate residual phases on individual lines of an electro-optic (EO) frequency comb. These demonstrations mark a significant step toward realizing narrowband filtering and high resolution shaping functionality in a scalable manner.

## Results

### SiP shaper design

Figure 1a is a high-level concept illustration of our SiP microresonator-based spectral shaper, and Fig. 1b displays its microscope image. A common bus waveguide routes an input broadband optical field to a bank of resonators. The input resonator bank downloads slices of the input spectrum and routes them through phase-shifting elements before finally uploading the slices onto a common output bus via the second resonator bank. Transmission spectra of both the input and output resonator banks can be accessed. The shapers are fabricated by SUNY Polytechnic through the foundry services offered by AIM Photonics<sup>43</sup> and wirebonded to a custom interposer and printed circuit board.

Resonators in our device (diagram in Fig. 1c) are designed using multimode waveguides. Operating these waveguides in the fundamental mode substantially diminishes the predominant loss mechanism of field-sidewall overlap in SiP waveguides, thereby ensuring low-loss performance<sup>44,45</sup>. The racetrack resonators include 200  $\mu\text{m}$ -long straight waveguides, which have a width of 2  $\mu\text{m}$ . These segments taper down to 1  $\mu\text{m}$ -wide waveguides, which feed into the bus-racetrack coupling region. This permits higher rates of coupling to the resonator, reducing the drop-port loss of the filter. To suppress higher-order mode excitation, the resonator and the bus waveguides follow an Euler curve<sup>44</sup>. The curve in the resonator reaches a minimum bending radius of 15  $\mu\text{m}$ , and the bus waveguides are designed to be phase-matched at the midpoint of the curve, where the local bending radius, width, and gap are 16  $\mu\text{m}$ , 0.64  $\mu\text{m}$ , and 0.18  $\mu\text{m}$ , respectively.

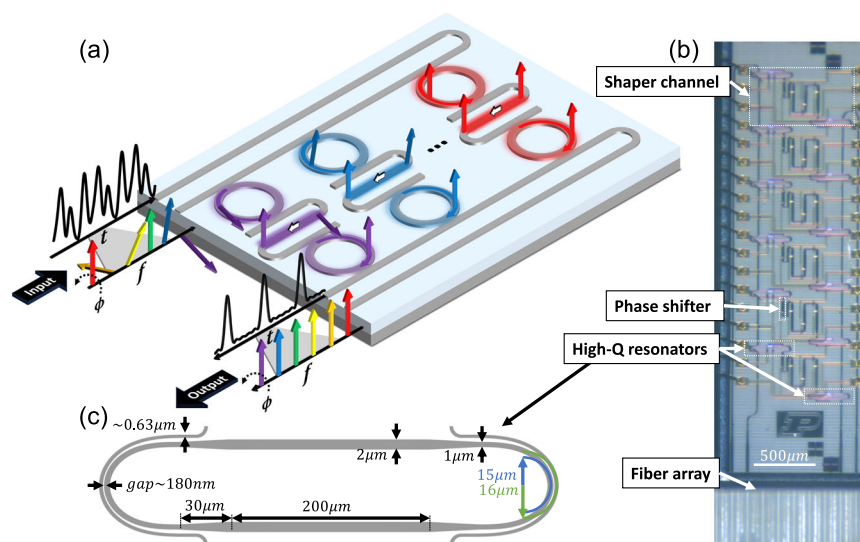


**Fig. 1 | Silicon photonic spectral shaper.** **a** Graphic illustration of a six-channel microresonator-based spectral shaper, and a conceptual illustration of line-by-line pulse shaping. An input optical frequency comb with random relative phases between comb lines generates a distorted waveform in the time domain. The

spectral shaper chip can be programmed to align the phases and produce transform-limited pulses at the output. **b** Top-down microscope image of the fabricated system. **c** Zoomed-in schematic of a single resonator device used in our shaper.

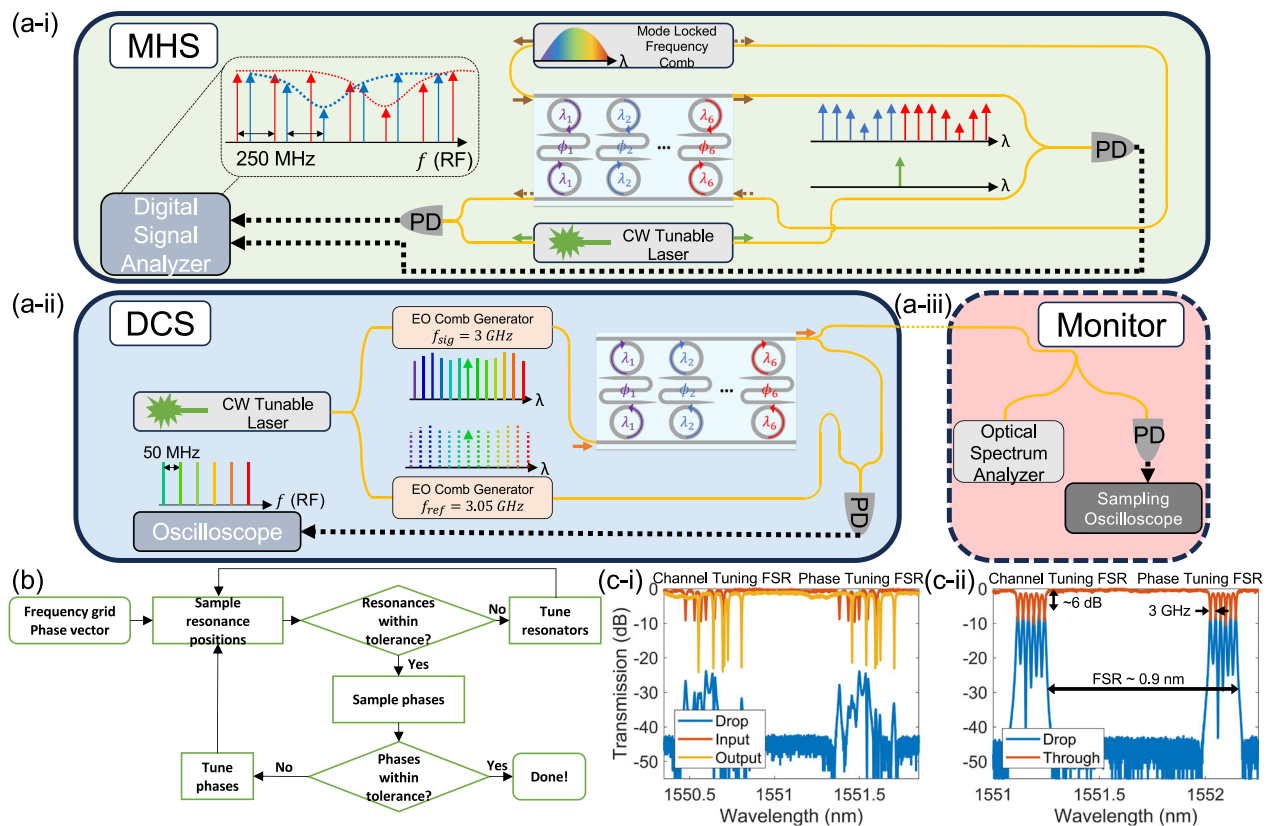


**Fig. 2 | Experimental configuration.** High-level schematic diagram of experimental setups for **a-i** Multi-Heterodyne Spectroscopy (MHS), **a-ii** Dual-Comb Spectroscopy (DCS), for measuring the channel frequencies and phases, respectively, and **a-iii** the Waveform Monitor. Yellow and dashed black lines indicate optical and RF connections, respectively. Brown (solid and dashed) and green arrows in **(a-i)** follow directions of propagation for the MLFC and CW laser, respectively. Orange arrows in **(a-ii)** follow the signal comb. Arrows on the resonators within the SiP shaper follow the direction of propagation for each method. For clarity, the SiP shaper is drawn here with optical I/O on both sides of the chip; in

the experiment, optical I/O is on a single side, as depicted in Fig. 1a. MHS and DCS measurements are run at the same time by adding circulators and DWDM filters. PD: Photodiode. **b** Flowchart of our shaper control scheme. **c-i** Transmission spectrum of the as-fabricated spectral shaper and **c-ii** with the shaper programmed to compress six lines from a 3 GHz EO comb. In both cases, the measurement is from a swept laser source and the two FSRs for MHS and DCS measurement are shown. Transmission is normalized to coupling loss to/from the chip, which we measure to be  $-3.5$  dB/facet.

A single resonator occupies a compact footprint of only  $0.045 \times 0.33$  mm<sup>2</sup>. Each resonator has a measured 3 dB linewidth, drop-port loss, and free spectral range (FSR) of  $-1.3$  GHz,  $-2.5$  dB, and  $-115$  GHz, respectively. We find average intrinsic and loaded quality factors of  $-6.15 \times 10^5$  and  $1.48 \times 10^5$  (see Supplementary Information note 2). Thermo-optic phase shifters comprised of doped silicon slabs functioning as resistive heating elements are placed between resonators in a channel and also embedded within each resonator for tuning the center frequency. Variable optical attenuators are also placed in-line within a channel for amplitude tuning although they are not used here. When resonators on the input and output sides are aligned to a common resonance mode, the composite shaper channel linewidth and drop-port loss are  $-900$  MHz and  $-6$  dB. Improved engineering of the resonator devices<sup>46,47</sup> and CMOS-compatible process quality refinements<sup>48,49</sup> may enable reduction in these quantities in future fabrication cycles.

The input and output resonators within any channel must have their center frequencies well-aligned to allow for efficient transmission of a spectral slice. Variation in silicon device layer thickness and sidewall roughness across a die leads to a starting resonant frequency mismatch between filters in a channel. Microheaters allow for thermal tuning of the resonant frequencies, but the simultaneous heating of devices leads to compounding thermal crosstalk making precise alignment challenging. For these reasons, and to exploit the tunability

of the resonators, a robust control method must be employed to align resonators within the shaper to specific frequency positions.

### MHS/DCS programming method

Figure 2a-i illustrates the experimental setup for the MHS measurement technique. We use a continuous wave (CW) laser and a stabilized mode-locked frequency comb (MLFC) for this purpose. We note that although the concept of MHS and multi-heterodyne beat generation also includes the beating between two frequency combs (i.e., DCS, which we adopt for phase measurement discussed later), we still designate this measurement as MHS to differentiate between this and the latter method. A portion of the spectrum from the MLFC is sent through bus waveguides on both the input and output sides of the shaper as indicated in Fig. 2a-i. The coupling between the bus waveguides and resonators leads to a significant ( $-10$  dB) frequency-dependent extinction as measured from the output of the bus waveguides, indicating the resonance frequencies of the resonators. In this way, the frequency response of the resonator bank is encoded onto the amplitude of the comb lines. By combining the spectrally modified comb exiting the bus waveguides with a CW laser operating at a fixed wavelength and beating on a high-speed photodetector (PD), the optical response of the resonator bank can be downconverted to the RF range after measurement by an oscilloscope and fast-Fourier transform (FFT). The optical spectrum is revealed as amplitude-

modified tones spaced at the repetition rate of the comb ( $f_{\text{rep}} = 250$  MHz). This MHS measurement enables multiple optical spectra to be measured at the same time (limited by the number of oscilloscope channels) and supports high rates of measurement, with a single measurement requiring an acquisition time on the order of  $\sim \mu\text{s}$ . Here, we employ this method to measure the optical spectrum of both resonator banks simultaneously (example spectra can be found in Supplementary Information note 4). By varying the resonator drive currents incrementally and processing the RF spectrum each time, the resonance frequencies of both resonators within each channel can be tracked via peak finding methods and tuned to arbitrary frequency positions relative to the CW laser and with a precision corresponding to the MLFC repetition rate. In our experiments, we align shaper channels to a uniformly spaced frequency grid.

To measure the spectral phase applied to each channel, we adopt a DCS method with two EO combs (schematic in Fig. 2a–ii) generated using the same pump laser. The two oscillators driving the combs are synchronized with each other. The signal comb is driven with a frequency equal to the spacing of the shaper channels ( $f_{\text{sig}}$ ) and the reference comb is driven at a slightly different frequency ( $f_{\text{ref}} = f_{\text{sig}} + \Delta f$ ). Signal comb modes on the high-wavelength side of the pump are sent through the shaper to accumulate the phase applied to each channel. The signal comb exiting the chip through the output port is combined with the reference comb and sent to a balanced PD. Heterodyne beats at harmonics of the dual-comb difference frequency ( $\Delta f$ ) are generated. The phase difference between the signal and reference comb can be measured by acquiring the generated electronic signal using an oscilloscope and sampling the phase at beat note frequencies after an FFT. Similar to MHS, the DCS measurement can be executed at MHz rates<sup>50</sup>. More details can be found in Methods and in Supplementary Information note 5.

The MHS and DCS measurements can be performed simultaneously in a bi-directional manner by employing circulators and dense wavelength division multiplexing (DWDM) filters. The periodic spectral response of the resonators permits a particular FSR to be used for MHS while an adjacent FSR is used for DCS phase measurement. We develop a Python-based control routine that takes as input a frequency grid and relative phase vector and iteratively performs MHS and DCS to track and align shaper channels onto the frequency grid and drive phase shifters to the appropriate relative phase values. The phase shifters are pre-driven with a power slightly higher than that to induce a  $\pi$ -phase shift at the start so that the drive can be increased or decreased to reach the desired phase. Likewise, the resonators are pre-tuned in a non-overlapping manner to simplify the alignment. The sequence of operations within the routine is shown in the flowchart of Fig. 2b. More details can be found in Methods and Supplementary Information note 6. The through and drop port transmission spectrum of the device before and after using this method to align channels to a 3 GHz grid with uniform phases is shown in Fig. 2c–i and Fig. 2c–ii, respectively. Note the FSRs used for both MHS and DCS are shown.

### Optical arbitrary waveform generation

For the OAWG and pulse compression applications that follow, we shape six lines of the signal comb used for DCS. The waveform monitor (red box in Fig. 2a–iii) is used to measure the optical spectrum and waveform in real time. The signal comb exiting the chip is split by a fiber coupler; half of the light is sent for DCS phase measurement while the other half is sent for temporal/spectral analysis using a 30 GHz PD and 50 GHz sampling oscilloscope and optical spectrum analyzer (OSA). Since the global phase of the output is unobservable in our application, we can automatically assign one of the six shaper phases to zero. Moreover, with the freedom to choose the time origin, any linear contribution to the spectral phase (equivalent to a group delay) can be ignored as well, allowing us to set a second phase shifter to zero.

In the context of the tests below, this flexibility allows us to apply zero drive to channels 3 and 6 without loss of functionality.

As a demonstration of the precise phase control achieved in our system, we generate a set of waveforms on a 3 GHz frequency grid from the six EO comb lines. The ideal waveforms we target, without factoring in our measurement system response, are presented in Fig. 3a, b, c–i to show the fine temporal features. The temporal profile of our initial phase state, with channels tuned to a 3 GHz grid and phase shifters driven to induce  $-\pi$  phase, is shown in Fig. 3a–ii (black dashed line). The corresponding measured phases for this untuned case (resonators aligned to 3 GHz grid and four phase shifters driven with  $-\pi$ ) are plotted in Fig. 3a–iii, which shows phase variation across each channel (excluding the two phase reference channels that are always set to zeros). The phase deviations could be caused by variations in tuning efficiency for each phase shifter, variations in optical path length for each channel caused by fabrication, or the input comb's nonuniform spectral phase profile. We adopt a commonly used normalized energy error (NEE) metric<sup>51</sup> to quantify similarity between target  $a(t)$  and measured  $d(t)$  waveforms as the ratio between the error  $e(t) = d(t) - a(t)$  and target waveform energy. For this waveform with untuned phases we find an NEE of 104.6%.

The waveform shows a significant difference after the shaper is programmed to achieve a uniform spectral phase, as shown in Fig. 3a–ii (blue line). We also include the ideal waveform (Fig. 3a–i) convolved with our measurement system impulse response in Fig. 3a–ii (orange trace), demonstrating excellent agreement with an NEE of 1.7% (see Methods for measurement of impulse response). Next, we target a phase vector implementing the temporal Talbot effect<sup>8</sup> where the phase modulation imposed on each line causes the temporal waveform to exhibit a multiplied repetition rate. We choose a phase vector (above Fig. 3b–i) such that the repetition rate is doubled. The various results for this phase state are shown in Fig. 3b–i, ii, iii. Finally, we program another state, which we term the forked state, with waveform and the phase vector shown in and above Fig. 3c–i. As before, the various results are shown in Fig. 3c–i, ii, iii. We note that the Talbot and forked states are more sensitive to phase accuracy than the compressed pulse. For these waveforms, unlike the compressed state, the phases on each line need to be fine-tuned to obtain the waveform closest to the theoretical prediction. This could be caused by an imperfect reference comb phase measurement and results in a target signal comb phase that is slightly different than the ideal signal comb phase (see Fig. 3b, c–iii). We measure  $< -28$  dB of nearest-neighbor crosstalk with a 3 GHz channel spacing, enabling the high-fidelity waveform generation (see Supplementary Information note 2). For all states, we see excellent agreement with the target in both the temporal waveform and measured spectral phase, with an NEE of 1.4 and 2.2% for Talbot and forked states, respectively.

### Pulse compression

We next show pulse compression for six-line combs with varying repetition rates of  $f_{\text{rep}} = 3, 4,$  and 5 GHz. Once the routine converges, the measured output pulses in the time domain are shown for the 3, 4, and 5 GHz repetition rates in Fig. 4a, b, c–i (blue trace), respectively. The measured waveforms are plotted alongside the simulated ideal waveforms taking into account the response of our measurement system as well as the optical power of the comb lines in Fig. 4a, b, c–i (orange trace). We compute an NEE of 2.1 and 2.3% for the 4 and 5 GHz compressed states, respectively. The measured power spectrum from the OSA (resolution  $\sim 1.25$  GHz) of the output comb for each repetition rate is shown in Fig. 4a, b, c–ii. The apparent difference in maximum power between the lines is primarily due to the non-flat region of the EO comb lines sent into the chip. Finally, the difference between the final measured spectral phases and the target phases are shown in Fig. 4a, b, c–iii. We see good agreement between the measured and

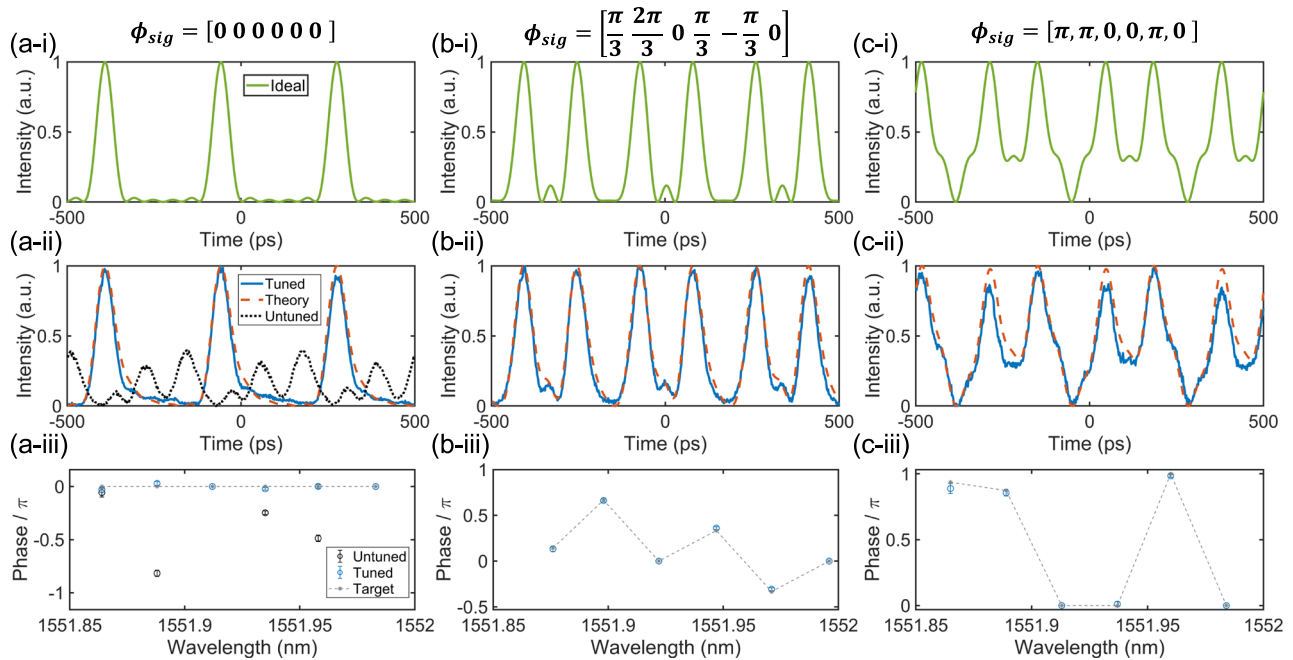


**Fig. 3 | Optical arbitrary waveform generation. a, b, c-i** Ideal target waveforms in the time domain (green traces) and signal comb spectral phase (top) for the compressed, Talbot, and forked state, respectively. **a, b, c-ii** Measured waveforms (blue trace) and the ideal waveforms convolved with the measurement system impulse response (dashed orange traces) for the compressed, Talbot, and forked states, respectively. An additional waveform is shown in **(a-ii)** (black dotted trace) with an untuned phase and phase shifters driven to induce  $-\pi$  phase. **a, b, c-iii** Target (gray dashed) and measured (blue scattered with error bars) signal comb spectral phase for the compressed, Talbot, and forked states, respectively. An

additional measurement is shown in **(a-iii)** (black scattered with error bars) for the untuned phase state, with phase shifters driven to induce  $-\pi$  phase. Figure legends in **(a-ii, iii)** are shared amongst subplots in a row, and the untuned state is only shown in **(a-ii, iii)**. All theoretical waveforms take into account the optical power of each comb line as measured by OSA. Error bars (standard deviation) in the phase plots are difficult to see. These errors always  $<0.15$  rad (see Methods and Supplementary Information note 6), and are on average  $-0.05$  rad. See Fig. 4a, b, c-iii for a clear example.

target temporal waveforms and spectral phases for each grid spacing, showcasing the tunability of our shaper.

## Discussion

Future shaper designs aim to improve the channel resolution (here  $\sim 900$  MHz), reduce channel insertion loss (here  $\sim 6$  dB), and increase the number of shaper channels. Improving the channel resolution relies in part on reducing the round trip loss in the resonators. Our micro-resonator intrinsic quality factor corresponds to an average propagation loss of  $\sim 1$  dB/cm. Compared to an average propagation loss of  $\sim 2.5$  dB/cm for 220 nm-thick SOI singlemode waveguides that the commercial foundry provides<sup>49</sup>, our multimode design results in a significant reduction of this loss, enabling higher quality factor. Modified resonator designs, such as increasing the length of the straight multimode waveguide segment<sup>46</sup> or adopting an adiabatic microring<sup>47</sup>, along with foundry process quality refinements<sup>48,49</sup>, have the potential to yield higher intrinsic quality factors on the order of  $10^6$ . In addition, other integrated material platforms such as  $\text{Si}_3\text{N}_4$ <sup>52</sup> and thin-film  $\text{LiNbO}_3$ <sup>53</sup>, with demonstrated ultra-low waveguide loss and high intrinsic Q factors in the order of  $10^7$  ( $10^8$  in  $\text{LiNbO}_3$ ), could potentially be adopted to attain a higher resolution. With further engineering of the coupling to the bus waveguides, the drop-port loss could be reduced at the same time. Minimizing the thermal crosstalk and power consumption can help scaling up of shaper channels. The addition of a substrate undercut, thermal trenching process<sup>54</sup>, the integration of phase change materials on SOI<sup>55</sup>, or using material platforms with intrinsic nonlinearities like  $\text{LiNbO}_3$ <sup>53</sup> or  $\text{AlGaAs}$ <sup>56</sup> could significantly reduce crosstalk effects and power consumption and simplify use of the shaper.

Our measurement process can be enhanced on the MHS side by both using a lower repetition-rate MLFC or using multiple CW laser lines (a DCS approach). The first modification would result in a finer

resolution measurement of the optical spectrum leading to more accurate channel alignment. The second would increase the measurable optical bandwidth allowing us to scale to larger channel numbers or spacings. Besides reducing the repetition rate of the MLFC, a spline or Lorentzian fit<sup>57</sup> could be applied to the MHS spectra to more accurately measure resonance frequencies. The DCS measurement can easily be scaled to accommodate a larger number of shaper channels by increasing the number of components in the EO comb generators or adding components for nonlinear spectral broadening<sup>58</sup>. Fast PDs ( $>200$  GHz) on the SOI platform have been demonstrated<sup>59</sup>, the integration of which could simplify the off-chip setup, while allowing for our tuning method to operate in a similar way. An FPGA, or monolithic electronic-photonic integration<sup>60</sup>, could replace oscilloscopes and embed electrical signal processing methods to reduce runtime. We note that the impetus for our control scheme was based on available equipment in our laboratory, and there are numerous other approaches for active control that could be useful for our system, for example involving dithering signals, photoconductive measurements, and phase interrogators<sup>61-63</sup>.

A comparison between our SiP shaper and state-of-the-art alternatives is helpful: a comprehensive list is presented in Table 1 and we proceed to discuss these and other pulse shaping systems. Commercial Fourier-transform pulse shapers today offer polarization independence and tunable channel bandwidths and amplitudes, yet are limited to  $\sim 10$  GHz resolution and  $\sim 5$  dB insertion loss (up to 2 dB increase below 15 GHz resolution)<sup>20</sup>. Bulk-optics Fourier shapers assembled in research laboratories have shown  $<400$  MHz resolution with an insertion loss of  $\sim 15$  dB<sup>4,23</sup>. On-chip Fourier-type shapers implementing AWGs have been shown in silica<sup>31,32</sup>,  $\text{InP}$ <sup>33,35</sup>, and  $\text{Si}_3\text{N}_4$ <sup>34</sup> platforms with typical channel bandwidths and losses in the 10s of GHz and  $\sim 10$  dB range, respectively. AWGs have also been used as

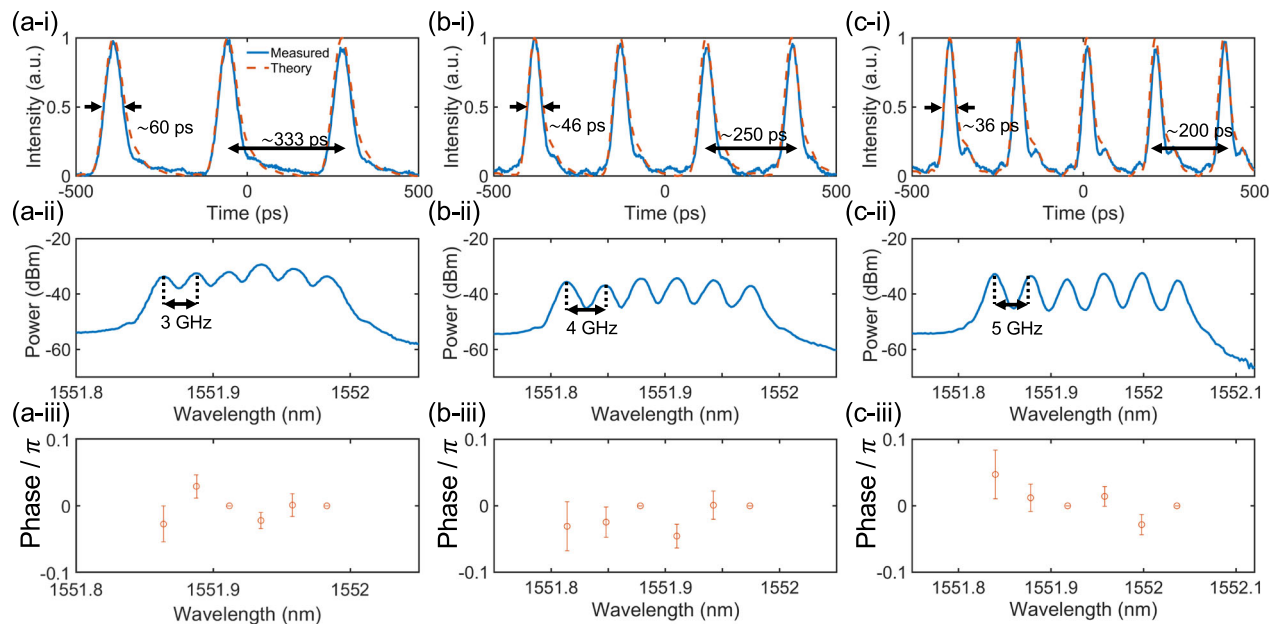


**Fig. 4 | Pulse compression.** **a, b, c-i** Waveforms acquired from a 30 GHz PD and 50 GHz sampling oscilloscope (blue traces) compared with the simulated target waveform after convolution with our measurement system impulse response (red dashed traces), for 3, 4, and 5 GHz channel spacing, respectively. **a, b, c-ii** OSA power spectral density of the EO comb lines coming out of the shaper after being

programmed for compression on 3, 4, and 5 GHz grids, respectively. The power measured here for each spectral line is taken into account in the theoretical trace in **(a, b, c-i)**. **a, b, c-iii** The difference between measured and target phase vectors with error bars (standard deviation) from the measured phases, after programming for 3, 4, and 5 GHz grids, respectively.

**Table 1 | State-of-the-art for Fourier-transform optical pulse shapers**

Fourier-Transform Pulse Shaper Comparison Table											
Technology	Spectral disperser	Demo.	Phase / Amp.	Total Chan.	Demo. Chan.	Chan. Loss (dB)	Chan. FWHM (GHz)	Chan. Spac. (GHz)	XT (dB)	Size (cm x cm)	Refs.
Bulk	Grating	LbL	Both	108	108	13	–	5	–	Benchtop	3
Bulk	VIPA/Grating	LbL	Phase	28	28	15	0.357	0.89	–14	Benchtop	4
Bulk	VIPA/Grating	LbL	Both	150	150	15	0.43	1	–	Benchtop	23
Silica/Bulk	AWG/Bulk	OSP <sup>a</sup>	Both	250	–	14	0.8	–	–	Benchtop	64
Silica	AWG	LbL	Both	64	32	–	–	20	–	4.4 × 8	31
Silica	AWG	LbL	Both	64	15	–15	–	10	–15	4.4 × 8	32
InP	AWG	LbL	Amp.	32	32	–	–	25	–13	–	33
Si <sub>3</sub> N <sub>4</sub> /InP	AWG	LbL	Phase	12	8	16 (4)	–	20	–12	–	34
InP	AWG	LbL	Both	100	8	31 (12)	6	10	–15	3 × 3.5	35
Si	MRR	Delay	Both	8	8	5 (22)	75	~125	–	–	38
Hydex	MRR	LbL	Phase <sup>b</sup>	4	4	– (4)	8	10	–	0.43 × 0.43	37
Si	MRR	LbL	Phase <sup>b</sup>	6	6	6 (7)	0.9	3	–28	0.27 × 0.08	This work

In column “Chan. Loss”, the on-chip loss of the device is presented with the total (fiber-to-chip + chip-to-fiber) coupling loss in the parenthesis. Acronyms: (VIPA) Virtually imaged phased array, (AWG) Arrayed-waveguide grating, (OSP) Optical Signal Processing, (MRR) Microring resonator, (LbL) Line-by-Line, (FWHM) Full-width at half-maximum, (XT) Crosstalk.

<sup>a</sup>OSP experiments involved all-optical Nyquist shaping and orthogonal frequency-division multiplexing (OFDM) subcarrier selection.

<sup>b</sup>Indicates control over both spectral phase and amplitude is possible but only one is demonstrated.

de(multiplexers) in tandem with free-space imaging systems and LCoS modulators to realize shapers with resolutions below 800 MHz<sup>64</sup>. Comparatively, non-Fourier shapers, based on Frequency Shifting Loops and (or) nonlinear optical techniques, have been shown with very high resolution (~10–100 MHz) and low losses<sup>12,13,15</sup>. However, the demonstrations in<sup>12,13</sup> are limited to generating complex waveforms based on a CW seed laser and cannot shape a broadband optical field. Nonlinear methods based on Stimulated Brillouin Scattering<sup>15</sup> are capable of operating on an arbitrary optical field, yet they rely on strong optical pump fields to generate sufficient Brillouin signals, which can impose additional requirements like, for example, significant pump suppression when operating on quantum light. In

contrast, our shaper is linear and is equally effective for both classical and quantum light<sup>65,66</sup>. Furthermore, our SiP shaper has, to the best of our knowledge, the highest resolution (channel linewidth 900 MHz) of any on-chip Fourier-transform pulse shaper to date (see Table 1). Combining our chip with advanced edge coupler designs<sup>67</sup> and photonic wirebonding techniques<sup>68</sup>, and fiber-to-fiber losses of our SiP shaper could be comparable to the commercial offering.

In conclusion, here we demonstrate a SiP spectral shaper with microresonator filter banks designed beyond the single-mode regime to achieve a high spectral resolution of ~900 MHz, a significant improvement over the bulk commercial counterpart with ~10 GHz resolution. In addition, we present an efficient method for adaptively

programming such shapers using common spectroscopy techniques and electrical signal processing methods. Our platform is well-suited for large-scale integration to produce the next generation of high resolution pulse shapers.

## Methods

### Multi-heterodyne spectroscopy

We spectrally filter a portion of a stabilized MLFC (Menlo Systems) with a 250 MHz repetition rate using a 100 GHz DWDM filter and send it through the bus waveguides in the shaper, as indicated by the brown arrows in Fig. 2a–i. The output comb with amplitude-modified lines is then combined with a CW laser fixed to emit at a wavelength near the targeted channel frequencies and fed to a PD to produce heterodyne beat notes. Erbium-doped fiber amplifiers (EDFAs) are used to amplify the optical signal prior to photodetection, along with DWDM filters to suppress amplified spontaneous emission (ASE). We use two 50 GHz PDs (u2tXPDV2020R, Coherent BPDV2120R) connected to a four-channel 30 GHz oscilloscope (80 GSFS, Keysight DSA93004L) to detect these beat notes. An FFT is performed on the oscilloscope after a 2  $\mu$ s acquisition and transferred via USB to a PC for processing. A single data transfer takes on the order of  $\sim$ 10 s of ms. RF tones are processed and resonance frequencies are identified using peak finding methods.

### Dual-comb spectroscopy

Signal and reference EO combs are generated by cascading a single intensity (JDS Uniphase, EOspace) and phase modulator (EOspace). Each comb generator is driven with an independent signal generator (Hittite HMC-T2100) with a repetition rate difference of  $\Delta f_{rep} = 50$  MHz. The signal generators are synchronized to a common clock (10 MHz). The intensity modulators are driven at an RF power that can produce a square-like pulse shape (amplitude of  $V_{\pi}/2$ )<sup>69</sup>. Approximately 26 dBm of RF power is provided to the phase modulator for each comb, leading to broadband combs spreading  $\sim$ 7 lines on each side of the pump (see Supplemental Information). RF amplifiers are used before the modulators to obtain the appropriate RF power levels. An RF phase shifter is included in each EO comb to align the phases between the intensity modulator and phase modulator. To ensure similar RF power levels for the 3, 4 & 5 GHz EO combs, and to align the phases between intensity and phase modulators, the detailed EO comb configurations (the number of RF amplifiers and the position of phase shifter) are different for each repetition rate. This is not a limitation to the method, but a requirement based on the available RF equipment.

The 2nd–7th signal comb lines at the higher wavelength side of the pump are sent to the chip. The signal comb going through the shaper and the MHS frequency comb going through a loopback are coupled out of the chip through the same waveguide but are spectrally separated with a DWDM filter. A portion of the output signal comb is then combined with the reference comb, detected on a 5 GHz balanced PD (Thorlabs BDX3BA), and is measured with a 2 GHz real-time oscilloscope (Rohde & Schwarz RTO1024). EDFAs are used to amplify the optical signal prior to photodetection, along with DWDM filters to suppress ASE. The scope acquires a 10  $\mu$ s signal, consisting of 500 interferogram periods (one interferogram period is  $1/\Delta f_{rep}$ ) between the two combs. The signal generator synchronization signal is used to trigger the oscilloscope to minimize the timing jitter between each measurement. FFT processing of the acquired signal provides the desired phase values. To achieve an accurate phase measurement, we process 16 acquisitions for each DCS measurement to obtain a mean and standard deviation of the extracted phases. A linear phase reference is necessary as acquisitions show slight timing jitter between measurements, affecting the mean and standard deviation of the phases. The error bars in the measured phase plots are the standard deviation, which is usually less than 0.1 rad and is not accepted unless  $<0.15$  rad. We note that the error bar of the 100 MHz-beat ( $\sim$ 0.1 rad, channel 1) is slightly higher than the other beats ( $\sim$ 0.08 rad for 150 MHz-beat,

channel 2, and  $\sim$ 0.05 rad for the other two beats, channels 4 and 5) possibly due to the low-frequency amplifier noise around  $<100$  MHz (See Fig. S9(c) in the Supplementary Information note 5).

### Control routine

The flowchart of the routine is shown in Fig. 2b. Resonators are tuned within tolerance when the error signal, the difference between measured resonance frequencies  $f$  and target frequencies  $F$ , satisfies  $Err_f = |F - f| < 250 \times 10^6$  Hz. Phases are tuned within tolerance when the error signal, the difference between the signal comb phases  $\phi_{sig}$  and target phases  $\phi_{target}$ , satisfies  $Err_\phi = |\phi_{target} - \phi_{sig}| < 0.1$  radians. The DCS measured phase vector is  $\phi_{DCS} = \phi_{sig} - \phi_{ref}$  (where  $\phi_{sig}$  and  $\phi_{ref}$  are absolute phase vectors of the signal and reference combs, respectively).  $\phi_{sig}$  can be controlled arbitrarily when an accurate value of  $\phi_{ref}$  is supplied (see Reference Comb Phase Measurement section in Methods for measurement details of  $\phi_{ref}$ ). As an example, for the pulse compression waveforms  $\phi_{sig} = 0$ , which means the DCS measured phase  $\phi_{DCS} = -\phi_{ref}$ . We approximate  $\phi_{ref}$  with quadratic frequency dependence and measure the quadratic coefficient to be  $-0.009$  rad/GHz<sup>2</sup>. Microheaters in the resonators and phase shifters are driven with linear steps in power proportional to the respective error signals  $Err_f$  and  $Err_\phi$ . The multichannel DC power supply (Nicslab XPOW-40AX-CCvCV-U-V12) updates drives in a serial fashion with a  $\sim$ ms setting time. Practically, the control routine takes a couple hundred iterations or just a few minutes to converge to the desired state (see Supplementary Information note 6 for an example). However, in scenarios where phases require fine-tuning like that described for the states in Fig. 3, the control sequence can be run once to converge near to the target state, and additional control sequences can be run with this state from the previous iteration as the starting point. In these cases, convergence to the next state can be reached in a few seconds.

### Reference Comb Phase Measurement

We program the shaper to pass only two channels. Two lines from the reference comb are sent through the chip, detected by a 30 GHz BPD (Thorlabs BDX3BA), and measured with a 50 GHz sampling oscilloscope (HP 54120). The sampling oscilloscope is triggered by a signal derived from the signal generator (using a 1/3 divider) driving the reference comb. The relative phase between the two comb lines is measured from the beat note as a temporal delay<sup>70</sup>. By tuning the pump laser wavelength in increments of the comb repetition rate, the relative phase difference between each adjacent pair of comb lines can be measured, and the spectral phase of the comb can be computed. A quadratic spectral phase provides a good fit to the measured values (see Supplementary Information note 5).

### Data availability

The datasets generated during this study are available from the corresponding author upon request.

### Code availability

The codes used throughout this work are available from the corresponding author upon request.

### References

- Cundiff, S. T. & Weiner, A. M. Optical arbitrary waveform generation. *Nat. Photonics* **4**, 760–766 (2010).
- Weiner, A. M. Ultrafast optical pulse shaping: a tutorial review. *Opt. Commun.* **284**, 3669–3692 (2011).
- Jiang, Z., Huang, C. B., Leaird, D. E. & Weiner, A. M. Optical arbitrary waveform processing of more than 100 spectral comb lines. *Nat. Photonics* **1**, 463–467 (2007).
- Willits, J. T., Weiner, A. M. & Cundiff, S. T. Line-by-line pulse shaping with spectral resolution below 890 mhz. *Opt. Express* **20**, 3110–3117 (2012).

5. Liao, S. et al. Arbitrary waveform generator and differentiator employing an integrated optical pulse shaper. *Opt. express* **23**, 12161–12173 (2015).
6. Divitt, S., Zhu, W., Zhang, C., Lezec, H. J. & Agrawal, A. Ultrafast optical pulse shaping using dielectric metasurfaces. *Science* **364**, 890–894 (2019).
7. Lin, I. S., McKinney, J. D. & Weiner, A. M. Photonic synthesis of broadband microwave arbitrary waveforms applicable to ultra-wideband communication. *IEEE Microw. Wirel. Compon. Lett.* **15**, 226–228 (2005).
8. Huang, C.-B., Jiang, Z., Leaird, D., Caraquiten, J. & Weiner, A. Spectral line-by-line shaping for optical and microwave arbitrary waveform generations. *Laser Photonics Rev.* **2**, 227–248 (2008).
9. Khan, M. H. et al. Ultrabroad-bandwidth arbitrary radiofrequency waveform generation with a silicon photonic chip-based spectral shaper. *Nat. Photonics* **4**, 117–122 (2010).
10. Zhang, W. & Yao, J. Silicon-based integrated microwave photonics. *IEEE J. Quantum Electron.* **52**, 1–12 (2015).
11. Wu, J. et al. RF photonics: an optical microcombs' perspective. *IEEE J. Sel. Top. Quantum Electron.* **24**, 1–20 (2018).
12. De Chatellus, H. G., Romero Cortés, L., Schnébelin, C., Burla, M. & Azaña, J. Reconfigurable photonic generation of broadband chirped waveforms using a single CW laser and low-frequency electronics. *Nat. Commun.* **9**, 1–12 (2018).
13. Schnébelin, C., Azaña, J. & Guillet de Chatellus, H. Programmable broadband optical field spectral shaping with megahertz resolution using a simple frequency shifting loop. *Nat. Commun.* **10**, 4654 (2019).
14. Pan, S. & Zhang, Y. Microwave photonic radars. *J. Lightwave Technol.* **38**, 5450–5484 (2020).
15. Redding, B., McKinney, J. D., Schermer, R. T. & Murray, J. B. High-resolution wide-band optical frequency comb control using stimulated brillouin scattering. *Opt. Express* **30**, 22097–22106 (2022).
16. Lu, H.-H. et al. Quantum interference and correlation control of frequency-bin qubits. *Optica* **5**, 1455–1460 (2018).
17. Kues, M. et al. Quantum optical microcombs. *Nat. Photonics* **13**, 170–179 (2019).
18. Lu, H.-H., Liscidini, M., Gaeta, A. L., Weiner, A. M. & Lukens, J. M. Frequency-bin photonic quantum information. *Optica* **10**, 1655–1671 (2023).
19. Weiner, A. M. Femtosecond pulse shaping using spatial light modulators. *Rev. Sci. Instrum.* **71**, 1929–1960 (2000).
20. Waveshapers - Programmable Optical Filters, howpublished = <https://www.coherent.com/networking/optical-instrumentation/waveshaper>, note = Accessed: 2024-02-20.
21. Xiao, S. & Weiner, A. M. An eight-channel hyperfine wavelength demultiplexer using a virtually imaged phased-array (VIPA). *IEEE Photonics Technol. Lett.* **17**, 372–374 (2005).
22. Lee, G.-H. & Weiner, A. M. Programmable optical pulse burst manipulation using a virtually imaged phased array (vipa) based fourier transform pulse shaper. *J. Lightwave Technol.* **23**, 3916–3923 (2005).
23. Lee, D. et al. Sub-GHz resolution line-by-line pulse shaper for driving superconducting circuits. *APL Photonics* **8**. <https://doi.org/10.1063/5.0157003> (2023).
24. Myilswamy, K. V. et al. Time-resolved hanbury brown–twiss interferometry of on-chip biphoton frequency combs using vernier phase modulation. *Phys. Rev. Appl.* **19**, 034019 (2023).
25. Ma, Y. et al. Precise pulse shaping for quantum control of strong optical transitions. *Opt. Express* **28**, 17171 (2020).
26. Stollenwerk, P. R., Antonov, I. O., Venkataramanababu, S., Lin, Y. W. & Odom, B. C. Cooling of a Zero-Nuclear-Spin Molecular Ion to a Selected Rotational State. *Phys. Rev. Lett.* **125**, 113201 (2020).
27. Meng, Z. & Yakovlev, V. V. Precise determination of brillouin scattering spectrum using a Virtually Imaged Phase Array (VIPA) spectrometer and Charge-Coupled Device (CCD) Camera. *Appl. Spectrosc.* **70**, 1356–1363 (2016).
28. Kabakova, I., Scarcelli, G. & Yun, S. H. *Brillouin light scattering in biological systems*, vol. 110 (Elsevier Inc., 2022).
29. Gatkine, P., Veilleux, S. & Dagenais, M. Astrophotonic spectrographs. *Appl. Sci.* **9**, 1–18 (2019).
30. Jovanovic, N. et al. 2023 astrophotonics roadmap: pathways to realizing multi-functional integrated astrophotonic instruments. *J. Phys. Photonics* **5**, 042501 (2023).
31. Fontaine, N. et al. 32 phase × 32 amplitude optical arbitrary waveform generation. *Opt. Lett.* **32**, 865–867 (2007).
32. Fontaine, N. K. et al. Compact 10 GHz loopback arrayed-waveguide grating for high-fidelity optical arbitrary waveform generation. *Opt. Lett.* **33**, 1714 (2008).
33. Metcalf, A. J. et al. Integrated line-by-line optical pulse shaper for high-fidelity and rapidly reconfigurable rf-filtering. *Opt. Express* **24**, 23925–23940 (2016).
34. Feng, S. et al. Rapidly reconfigurable high-fidelity optical arbitrary waveform generation in heterogeneous photonic integrated circuits. *Opt. Express* **25**, 8872 (2017).
35. Soares, F. M. et al. Monolithic inp 100-channel × 10-ghz device for optical arbitrary waveform generation. *IEEE Photonics J.* **3**, 975–985 (2011).
36. Gehl, M. et al. Active phase correction of high resolution silicon photonic arrayed waveguide gratings. *Opt. Express* **25**, 6320–6334 (2017).
37. Agarwal, A. et al. Fully programmable ring-resonator-based integrated photonic circuit for phase coherent applications. *J. Lightwave Technol.* **24**, 77–87 (2006).
38. Wang, J. et al. Reconfigurable radio-frequency arbitrary waveforms synthesized in a silicon photonic chip. *Nat. Commun.* **6**, 5957 (2015).
39. Onural, D., Gevorgyan, H., Zhang, B., Khilo, A. & Popović, M. A. in *Frontiers in Optics + Laser Science 2021. Technical Digest Series* (eds Mazzali, C., Poon, T. (T.-C.), Averitt, R. & Kaindl, R.) FTh6B.4 (Optica Publishing Group, 2021).
40. Cohen, L. M. et al. Fine-resolution silicon photonic wavelength-selective switch using hybrid multimode racetrack resonators. *J. Lightwave Technol.* **42**, 4503–4510 (2024).
41. Urabe, K. & Sakai, O. Multiheterodyne interference spectroscopy using a probing optical frequency comb and a reference single-frequency laser. *Phys. Rev. A* **88**, 023856 (2013).
42. Coddington, I., Newbury, N. & William, S. Dual-comb spectroscopy. *Optica* **3**, 414–426 (2016).
43. Fahrenkopf, N. M. et al. The AIM photonics MPW: a highly accessible cutting edge technology for rapid prototyping of photonic integrated circuits. *IEEE J. Sel. Top. Quantum Electron.* **25**, 1–6 (2019).
44. Zhang, L. et al. Ultrahigh-Q silicon racetrack resonators. *Photonics Res.* **8**, 684 (2020).
45. Cohen, L. M. et al. Low-loss, high finesse, add-drop resonators from a commercial silicon photonics foundry. In *2022 IEEE Photonics Conference (IPC)* 1–2 (IEEE, 2022).
46. Onural, D., Gevorgyan, H., Zhang, B., Khilo, A. & Popović, M. A. Ultra-high Q Resonators and Sub-GHz Bandwidth Second Order Filters in an SOI Foundry Platform. *Ofc* **2020** **1**, 5–7 (2020).
47. Nijem, J. et al. High-Q and high finesse silicon microring resonator. *Opt. Express* **32**, 7896 (2024).
48. Fanto, M. L. Quantum integrated photonics fabrication at the foundry level. <https://doi.org/10.1117/12.2603533> (2021).
49. Carpenter, L. G. et al. Low losses in an active silicon photonic multi-project wafer runs **12006**, 3 (2022).
50. Durán, V., Tainta, S. & Torres-Company, V. Ultrafast electrooptic dual-comb interferometry. *Opt. Express* **23**, 30557 (2015).
51. Scott, R. P., Fontaine, N. K., Heritage, J. P. & Yoo, S. J. Dynamic optical arbitrary waveform generation and measurement for telecommunications. *Opt. Express* **18**, 18655–18670 (2010).



52. Liu, J. et al. High-yield, wafer-scale fabrication of ultralow-loss, dispersion-engineered silicon nitride photonic circuits. *Nat. Commun.* **12**, 2236 (2021).
53. Shams-Ansari, A. et al. Reduced material loss in thin-film lithium niobate waveguides. *APL Photonics* **7**, 081301 (2022).
54. van Niekerk, M. et al. Wafer-scale-compatible substrate undercut for ultra-efficient SOI thermal phase shifters. In *Conference on Lasers and Electro-Optics, Technical Digest Series, Paper JTh3B.24* (Optica Publishing Group, 2022).
55. Ríos, C. et al. Ultra-compact nonvolatile phase shifter based on electrically reprogrammable transparent phase change materials. *Photonix* **3**, 26 (2022).
56. Chiles, J. et al. Multifunctional integrated photonics in the mid-infrared with suspended algaas on silicon. *Optica* **6**, 1246–1254 (2019).
57. Feng, S. et al. Silicon photonics: From a microresonator perspective. *Laser Photonics Rev.* **6**, 145–177 (2012).
58. Torres-Company, V. & Weiner, A. M. Optical frequency comb technology for ultra-broadband radio-frequency photonics. *Laser Photonics Rev.* **8**, 368–393 (2014).
59. Lischke, S. et al. Ultra-fast germanium photodiode with 3-dB bandwidth of 265 GHz. *Nat. Photonics* **15**, 925–931 (2021).
60. Atabaki, A. H. et al. Integrating photonics with silicon nanoelectronics for the next generation of systems on a chip. *Nature* **556**, 349–353 (2018).
61. Padmaraju, K. et al. Wavelength locking and thermally stabilizing microring resonators using dithering signals. *J. Lightwave Technol.* **32**, 505–512 (2014).
62. Jayatilaka, H., Shoman, H., Chrostowski, L. & Shekhar, S. Photoconductive heaters enable control of large-scale silicon photonic ring resonator circuits. *Optica* **6**, 84–91 (2019).
63. Kjellman, J. O. et al. Densely integrated phase interrogators for low-complexity on-chip calibration of optical phased arrays. *J. Lightwave Technol.* **40**, 5660–5667 (2022).
64. Rudnick, R. et al. Sub-ghz resolution photonic spectral processor and its system applications. *J. Lightwave Technol.* **35**, 2218–2226 (2017).
65. Nussbaum, B. E., Pizzimenti, A. J., Lingaraju, N. B., Lu, H.-H. & Lukens, J. M. Design methodologies for integrated quantum frequency processors. *J. Lightwave Technol.* **40**, 7648–7657 (2022).
66. Lu, H.-H., Lingaraju, N. B., Leaird, D. E., Weiner, A. M. & Lukens, J. M. High-dimensional discrete fourier transform gates with a quantum frequency processor. *Opt. Express* **30**, 10126–10134 (2022).
67. Mu, X., Wu, S., Cheng, L. & Fu, H. Edge couplers in silicon photonic integrated circuits: a review. *Appl. Sci.* **10**, 1538 (2020).
68. Blaicher, M. et al. Hybrid multi-chip assembly of optical communication engines by in situ 3d nano-lithography. *Light Sci. Appl.* **9**, 71 (2020).
69. Wu, R., Supradeepa, V. R., Long, C. M., Leaird, D. E. & Weiner, A. M. Generation of very flat optical frequency combs from continuous-wave lasers using cascaded intensity and phase modulators driven by tailored radio frequency waveforms. *Opt. Lett.* **35**, 3234 (2010).
70. Jiang, Z., Leaird, D. E. & Weiner, A. M. Optical arbitrary waveform generation and characterization using spectral line-by-line control. *J. Lightwave Technol.* **24**, 2487–2494 (2006).

## Acknowledgements

The authors would like to thank Jason D. McKinney and Joseph M. Lukens for reviewing the manuscript, Vivek Wankhade for helpful discussions, and Matthew van Niekerk and Stefan Preble for providing wirebonding

materials. This work was supported by the National Science Foundation (NSF) grant (2034019-ECCS), the Air Force Office of Scientific Research (AFOSR) grants (FA8750-20-P-1705 and FA9550-20-1-0283), and an Oak Ridge National Laboratory (ORNL) subcontract (4000151703). Navin B. Lingaraju acknowledges independent research and development support from The Johns Hopkins Applied Physics Laboratory. This manuscript is among the last that the late Andrew M. Weiner worked on prior to his death. We are deeply grateful for his guidance, wisdom, and attention to detail, and we mourn his loss and look to further his legacy in our work. His obituary may be found in *Nat. Photon.* **18**, 400–401 (2024). Publication of this article was funded in part by Purdue University Libraries Open Access Publishing Fund.

## Author contributions

L.M.C. designed the chip and conceived the methods. L.M.C., K.W., K.V.M., and S.F. contributed to the experimental setup. L.M.C. and K.W. carried out the experiments. L.M.C., K.W., and K.V.M., drafted the manuscript. N.B.L. and A.M.W. initialized the project. A.M.W. supervised the work. All authors discussed the results and contributed to the writing of the manuscript.

## Competing interests

The authors declare no competing interests.

## Additional information

**Supplementary information** The online version contains supplementary material available at <https://doi.org/10.1038/s41467-024-52051-9>.

**Correspondence** and requests for materials should be addressed to Lucas M. Cohen or Kaiyi Wu.

**Peer review information** *Nature Communications* thanks Xingjun Wang, and the other, anonymous, reviewer(s) for their contribution to the peer review of this work. A peer review file is available.

**Reprints and permissions information** is available at <http://www.nature.com/reprints>

**Publisher's note** Springer Nature remains neutral with regard to jurisdictional claims in published maps and institutional affiliations.

**Open Access** This article is licensed under a Creative Commons Attribution-NonCommercial-NoDerivatives 4.0 International License, which permits any non-commercial use, sharing, distribution and reproduction in any medium or format, as long as you give appropriate credit to the original author(s) and the source, provide a link to the Creative Commons licence, and indicate if you modified the licensed material. You do not have permission under this licence to share adapted material derived from this article or parts of it. The images or other third party material in this article are included in the article's Creative Commons licence, unless indicated otherwise in a credit line to the material. If material is not included in the article's Creative Commons licence and your intended use is not permitted by statutory regulation or exceeds the permitted use, you will need to obtain permission directly from the copyright holder. To view a copy of this licence, visit <http://creativecommons.org/licenses/by-nc-nd/4.0/>.

© The Author(s) 2024